

FY20 Laboratory Basic Science Program

M. S. Wei

Laboratory for Laser Energetics, University of Rochester

In FY20, 22 Laser Basic Science (LBS) projects were allocated a total of 21.5 shot days for experiments at the Omega Laser Facility. A total of 186 target shots were conducted for sixteen LBS projects led by scientists from Lawrence Livermore National Laboratory (LLNL), Los Alamos National Laboratory (LANL), Lawrence Berkeley National Laboratory (LBNL), Princeton Plasma Physics Laboratory (PPPL), SLAC, and LLE (see Table I). The FY20 LBS experiments are summarized here.

Table I: LBS experiments conducted at the Omega Laser Facility in FY20.

Principal Investigator	Institution	Title
F. Albert	LLNL	X-Ray Radiation Driven by Laser Wakefield Acceleration at OMEGA EP
H. Chen	LLNL	Develop a Magnetic Mirror Trap for Laser-Produced Relativistic Electron-Positron Pairs
H. Chen	LLNL	Laboratory Model of Particle Acceleration in Supernova Shocks
F. Coppari*	LLNL	The Atomic Structure and Melting of New Solid and Superionic Water Ices at Multi-Megabar Pressures: Searching for Ice XIX
T. Doepfner	LLNL	Experimental Measurement of Mutual Diffusivity in Warm Dense Matter
K. Flippo	LANL	Quantifying the Path to Saturation in a Turbulent Magnetic Dynamo
W. Fox	PPPL	Turbulent Transport in Magnetized HED Plasmas
D. E. Fratanduono	LLNL	Investigating Giant Impacts Between Rocky Planets with High-Pressure Melting and Shock Equation-of-State Measurements on Complex Silicates
L. Gao	PPPL	Effect of Laser Parameters on Magnetic Field Generation with Laser-Powered Capacitor Coils
A. Gleason	SLAC	Viscosity Measurements Using Tracer Particles
S. Jiang	LLNL	Characterizing Pressure Ionization in High-Density with X-Ray Line Emission Spectroscopy
O. M. Mannion	LLE	Measuring the Gamow Energy Shift of Fusion Products in High-Temperature Plasmas
M. Millot*	LLNL	Peering into the Ices Giant Planets Using Shocks On Pre-Compressed Water-Ammonia Mixtures: Superionic Ammonia Hydrates
Z. L. Mohamed*	LLE	Study of Gamma-Ray Products from Reactions Relevant to Big Bang Nucleosynthesis
P. M. Nilson	LLE	Terra Incognita: Testing the Predictions of Density Functional Theory (DFT) in Warm and Extremely Dense Plasmas
A. Pak*	LLNL	Proton Radiography of Target Normal Sheath Acceleration Fields in the Long-Pulse Regime
H. G. Rinderknecht*	LLE	Measuring the Triton Breakup Reaction T(n,2n)D
R. Saha and J. R. Rygg*	LLE	Optical and X-Ray Scattering Measurements of Dense Lithium

Table I: LBS experiments conducted at the Omega Laser Facility in FY20 (continued).

Principal Investigator	Institution	Title
R. Smith	LLNL	The Effect of Alloying on High-Pressure Phase Transformations: Diffusion Time Scales and Kinetics
C. Stoeckl	LLE	Development of New Experimental Platform LIANS on OMEGA EP for Deuteron- and Triton-Induced Nuclear Reactions
S. Zhao	LBNL	Extreme Deformation and Failure of High-Entropy Alloys by Laser Shock-Induced Compression and Tension
A. B. Zystra	LLNL	Implosions for Studying Solar CNO Reactions

*Six FY20 LBS projects were postponed with shots rescheduled in FY21.

During FY20, LLE issued a solicitation for LBS proposal for beam time in FY21. A total of 36 proposals were submitted requesting a total of 56 shot days, 260% exceeding the LBS allocation, showing strong interest and high demand of Omega facility time for basic high-energy-density (HED) science experiments from both National Nuclear Security Administration Inertial Confinement Fusion (NNSA ICF) and Office of Science laboratories. An independent LBS Proposal Review Committee consisting of 12 experts from university, national labs, and industry reviewed and ranked the proposals. Based on the Review Committee’s recommendation, 22 proposals were selected and allocated a total of 22.5 shot days (including one additional day from the contingency pool) for experiments at the Omega Laser Facility in FY21 as shown in Table II.

Table II: LBS experiments approved for target shots at the Omega Laser Facility in FY21.

Principal Investigator	Lead Institution	Title
F. Albert	LLNL	X-Ray Radiography with Sources Driven by Laser Wake-Field Acceleration
H. Chen	LLNL	Develop a Magnetic Mirror Trap for Laser-Produced Relativistic Electron–Positron Pairs
H. Chen	LLNL	Measuring Particle Transport in Turbulent Plasmas
F. Coppari	LLNL	Melting, Polymorphism, and Kinetics of Crystallization of Superionic Ice
T. Doepfner	LANL	Developing Fresnel Diffractive Radiography for Mutual Diffusion Measurements
C. J. Forrest	LLE	Inelastic Reactions of 14-MeV Neutrons from Lithium Isotopes
D. E. Fratanduono	LLNL	Investigating Giant Impacts on Rocky Planets with High-Pressure Melting and Shock Equation-of-State Measurements on Complex Silicates
L. Gao	PPPL	Investigation of Magnetic-Field Generation with Short-Pulse Laser-Powered Capacitor Coils
Y.-J. Kim	LLNL	Extreme Chemistry Inside Icy Planets: Shock Compression of Precompressed Ammonia–Water Mixtures
N. Lemos	LLNL	Proton Radiography of a Hybrid Laser Wakefield Accelerator Driven by a Picosecond, Kilojoule-Class Laser
L. Masse	LLNL	Evidencing the Transition from Landau–Darrieus Instability to Ablative Richtmyer–Meshkov Using Low-Density Foam Targets on OMEGA EP
P. M. Nilson	LLE	Atomic Physics at Petapascal Pressures
J. L. Peebles	LLE	Comparison and Validation of Dynamic Magnetic-Field Diagnostics on Laser-Driven Coils and MIFEDS
H. G. Rinderknecht	LLE	A Plasma Rectifier for Extreme Magnetic Fields, Efficient Electron Acceleration, and Bright X-Ray Sources
S. Singh	LLNL	Determination of High-Pressure Phase Transformation Mechanisms at the Atomic Scale

Table II: LBS experiments approved for target shots at the Omega Laser Facility in FY21 (continued).

Principal Investigator	Lead Institution	Title
V. A. Smalyuk	LLNL	The Kelvin–Helmholtz Instability with a Magnetic Twist
C. Stoeckl	LLE	Development of New Experimental Platform LIANS on OMEGA EP for Deuteron and Triton-Induced Nuclear Reactions
G. Tabak	LLE	Extreme Physics of Hydrogen and Water in Planetary Interiors
W. Theobald	LLE	X-Ray Phase-Contrast Imaging of Imploding Strong Shock Waves
T. J. Weber	LANL	Understanding Collisional Interpenetration of Ion Species with Talbot–Lau Interferometry
S. Zhao	LBNL	Extreme Deformation of High-Entropy Alloys
A. B. Zylstra	LLNL	Big-Bang Nucleosynthesis Relevant to the Primordial ${}^7\text{Li}$ Problem

Development of Self-Modulated Laser Wakefield Acceleration on OMEGA EP

Principle Investigators: F. Albert, P. M. King,* N. Lemos, J. Williams, and H. Chen (LLNL); J. L. Shaw and D. H. Froula (LLE); and M. Sainclair and C. Joshi (University of California, Los Angeles)

*Also University of Texas, Austin

X-ray backlighting is one of the most commonly used methods to look into the extreme temperatures, pressures, and densities created during laser-driven high-energy-density science (HEDS) experiments. Over the years, much effort has gone into developing backlighting techniques to look into these states of matter, with new sources and diagnostics. The properties of an x-ray backlighter (flux, source size, spectrum, duration) required for an experiment depend on the application being studied and on the quantity being measured. The goal of the Wakefield-EP shot series is to develop a new type of x-ray source that could be advantageous for applications requiring broadband spectra, small source sizes (sub-50 μm), short duration (less than 10 ps), and x rays extending beyond 100 keV. Our proposed x-ray sources are based on laser wakefield acceleration (LWFA) of electrons in the self-modulated regime (SMLWFA). Specifically, we aim to develop three different x-ray sources based on betatron radiation, Compton scattering, and bremsstrahlung emission.

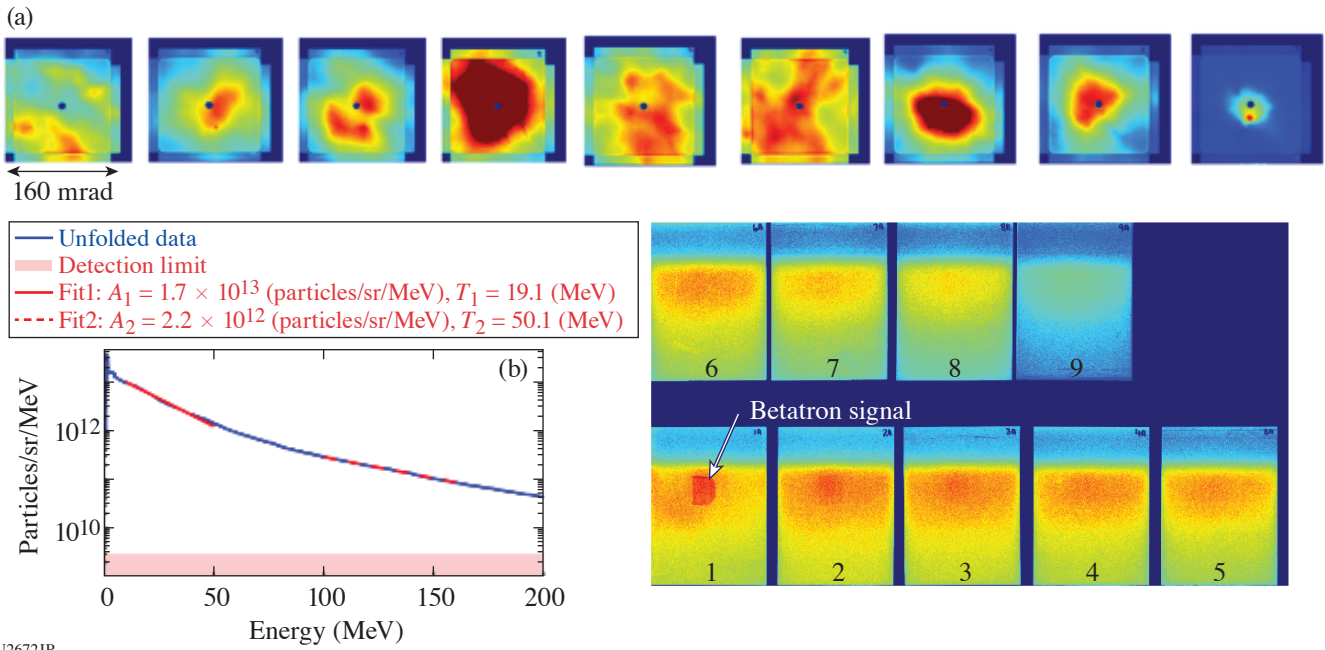
The WakefieldLBS-EP-20A shot day aimed at producing and detecting betatron radiation produced by SMLWFA using a modified version of the electron–positron proton spectrometer (EPPS) diagnostic. The modified EPPS used apertures enlarged to 5 mm (instead of 1 mm) and included a hole at the back of the magnet box, as well as a stack of nine image plates at the back of the ten-inch–manipulator (TIM) cart to detect betatron radiation. Initial analysis of these experiments shows that EPPS was successful at simultaneously recording electron, spectrum, profile, and x-ray data (Fig. 1).

The wakefield platform produced robust electron beam data, recording a >100-nC charge electron beam at each shot, as well as two-temperature spectra extending up to about 200 MeV (Fig. 1). Our data show that our signal-to-noise ratio needs to be improved for more-efficient x-ray detection. With the help of Monte Carlo simulations, we are working on additional diagnostic shielding enhancements for our next shot day in February 2021.

Developing a Magnetic Mirror Trap for Laser-Produced Relativistic Electron–Positron Pairs

Principle Investigators: H. Chen, J. von der Linden, M. Edwards, and A. Link (LLNL); G. Fiksel and L. Willingale (University of Michigan); and J. L. Peebles (LLE)

Creating a relativistic electron–positron pair plasma in a laboratory is of great interest to basic plasma science and to laboratory astrophysics experiments that explore particle acceleration through collisionless shocks. The difficulties of such an endeavor are caused by the limited number of pairs that can be created and the limited strength of magnetic field that is necessary for the pair confinement.^{1,2} Using the award under the Laboratory Basic Science program, we designed and tested a mirror trap for laser-produced relativistic pairs.

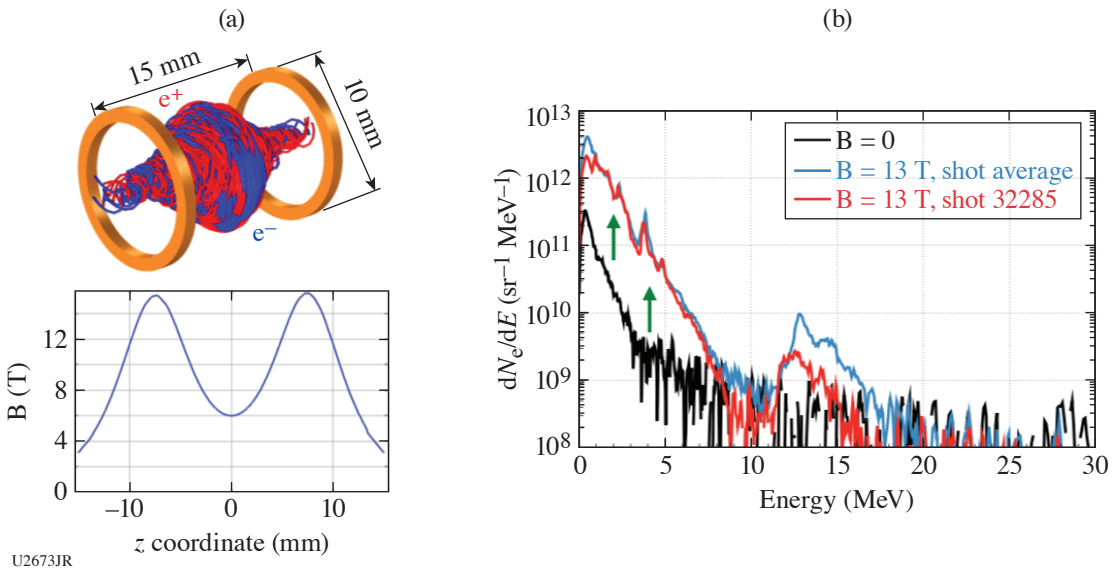


U2672JR

Figure 1

Results obtained during the Wakefield LBS-EP-20A shot day using the modified EPPS diagnostic. (a) An electron beam profile for each of our nine shots; (b) representative electron beam spectrum; (c) betatron x-ray signal measured on the rear image-plate stack of EPPS.

A schematic of the magnetic trap [shown in Fig. 2(a)] consists of the LLE’s magneto-inertial fusion electrical discharge system (MIFEDS) and a pair-generating target placed inside the magnetic mirrors. The target is irradiated by a high-intensity laser beam; the positrons and electrons are generated and, depending on their energy, will be either confined by the mirror magnetic field or allowed to escape. With the magnetic field at the mirror center at about 7 T, the simulations show that the trap can confine



U2673JR

Figure 2

(a) A magnetic mirror formed by MIFEDS can trap the low-energy (<3 -MeV) pairs according to simulation. (b) Experimental data show that $E < 3$ MeV have indeed been well confined and only escape axially, the axial flux of $3 \text{ MeV} < E < 15 < \text{MeV}$ is increased, and 15-MeV particles are focused by the magnetic field in this configuration.

particles with a kinetic energy of less than 3 MeV, while particles with higher energies will partially or totally escape after one or more gyrations.

The experimental results appear to confirm these simulations, as shown in Fig. 2(b). The confinement studies were performed on electrons in this first experiment due to their higher numbers and easier detection. In principle, the positrons should behave the same as the electrons at the same energies, albeit having the opposite direction of rotation. Figure 2(b) shows clearly that with the magnetic field on, the axial flux of the low-energy electrons generated inside the trap is greatly increased, indicating that they are well confined in the radial direction and eventually only escape axially, as predicted.³

Investigating Giant Impacts Between Rocky Planets with Shock Equation-of-State Measurements on Natural Silicates

Principle Investigators: B. A. Chidester and S. T. Stewart (University of California, Davis); M. Millot and D. E. Fratanduono (LLNL); J. P. Townsend (SNL); and J. Li (University of Michigan)

The Earth and other rocky planets likely formed after a series of energetic collisions in the early solar system. Simulations of these impacts rely on accurate equations of state and phase diagrams of natural materials to determine the amount of melting, vaporization, and mixing that occurs in the aftermath of a giant impact. Combined with data collected at the Sandia Z Machine, this study is the first to measure the principal pressure–density–temperature ($P\rho T$) Hugoniot of the most-abundant minerals in Earth's upper mantle—olivine [(Mg_{0.9},Fe_{0.1})₂SiO₄] and orthopyroxene [(Mg_{0.9},Fe_{0.1})SiO₃]—to conditions relevant to giant impacts. Additionally, we collected the first shock-temperature measurements on wadsleyite, a high-pressure polymorph of olivine that exists in Earth's transition zone.

We completed 15 shots on OMEGA EP in the one-day allocation, using alternating beams to increase the shot rate. Those data are combined with data collected in a previous shot allocation (FY19-SilicateEOS). As shown in Fig. 3(a), the olivine shock temperatures measured on OMEGA EP match those measured on the Sandia Z Machine and quantum molecular dynamics calculations. In Fig. 3(b), we show that natural olivine is very similar to synthetic forsterite, the magnesium endmember of this material (Mg₂SiO₄) (Ref. 4). $P\rho T$ data on wadsleyite will provide a wealth of thermodynamic information for the olivine series, including the Grüneisen parameter that describes thermal pressure. The data collected on natural orthopyroxene will complement our previous work on enstatite (MgSiO₃) (Ref. 5). All of these data will be incorporated into analytical equations of state (ANEOS) for use in planetary impact simulations [dashed orange curve, Fig. 3(b)].⁶

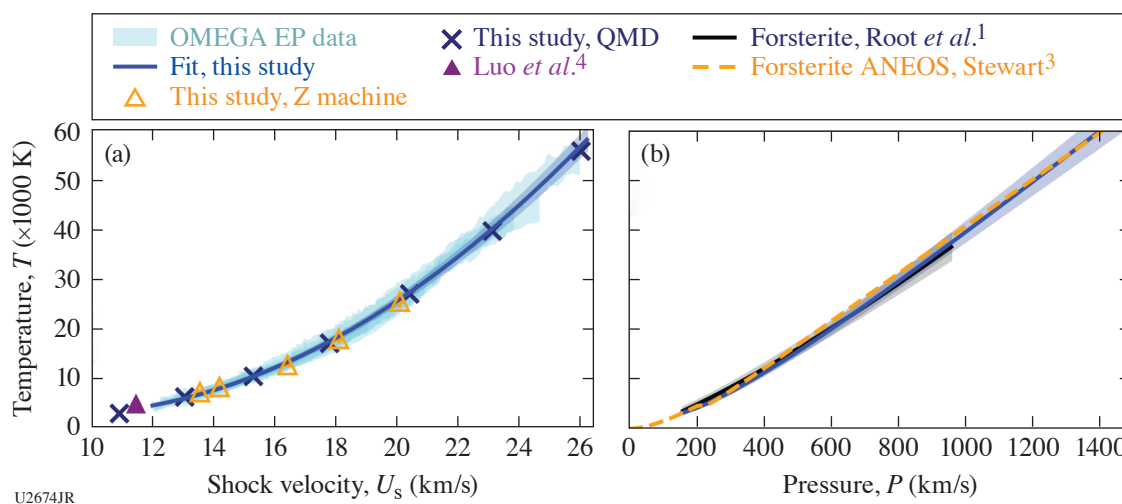


Figure 3

(a) $T-U_s$ data for natural olivine. Fit to OMEGA EP data in blue; data collected at the Sandia Z machine, on a gas gun (purple triangle);⁷ and quantum molecular dynamics simulations (\times 's) included for comparison. (b) $T-P$ curve on the olivine Hugoniot. Forsterite Hugoniot from Root *et al.* (2018);⁴ new forsterite ANEOS from Stewart (2019)⁶ included for comparison.

Fresnel Diffractive–Refractive Radiography for Measurements of Mutual Diffusivity in Warm Dense Matter

Principal Investigators: T. Döppner, O. L. Landen, Y. Ping, L. Divol, and A. Saunders (LLNL); T. G. White, C. H. Allen, and M. Oliver (University of Nevada, Reno); and W. Theobald (LLE)

The experimental measurement of concentration-driven diffusion between two species in warm dense matter (WDM) is important for benchmarking instability growth simulations in ICF experiments.⁸ The scale length of this mutual diffusion is of the order of $1\ \mu\text{m}$, necessitating a diagnostic tool that can resolve density-gradient changes with sub- $1\text{-}\mu\text{m}$ resolution. With two half-day campaigns on OMEGA-60 this year, we have developed a reliable x-ray radiography technique that is sensitive to Fresnel diffraction signatures by using novel $1\text{-}\mu\text{m}$ -wide slits, which we have termed Fresnel diffractive–refractive radiography (FDR) [Fig. 4(a)].

Over two half-days, our experiments—MutualDiffusion-20A&B on OMEGA-60—progressed from imaging cold wire targets to sampling driven dynamic WDM systems, looking at the interface of isochorically heated Al and CH [(Figs. 4(b) and 4(c)]. Our preliminary analysis indicates that we captured changes in the CH as it expands, but further analysis is required to determine the change in the Al–CH interface. With an upcoming campaign on OMEGA-60 in February 2021, we plan to further refine the platform before converting it for use at the National Ignition Facility (NIF) for campaigns in FY22 and beyond.

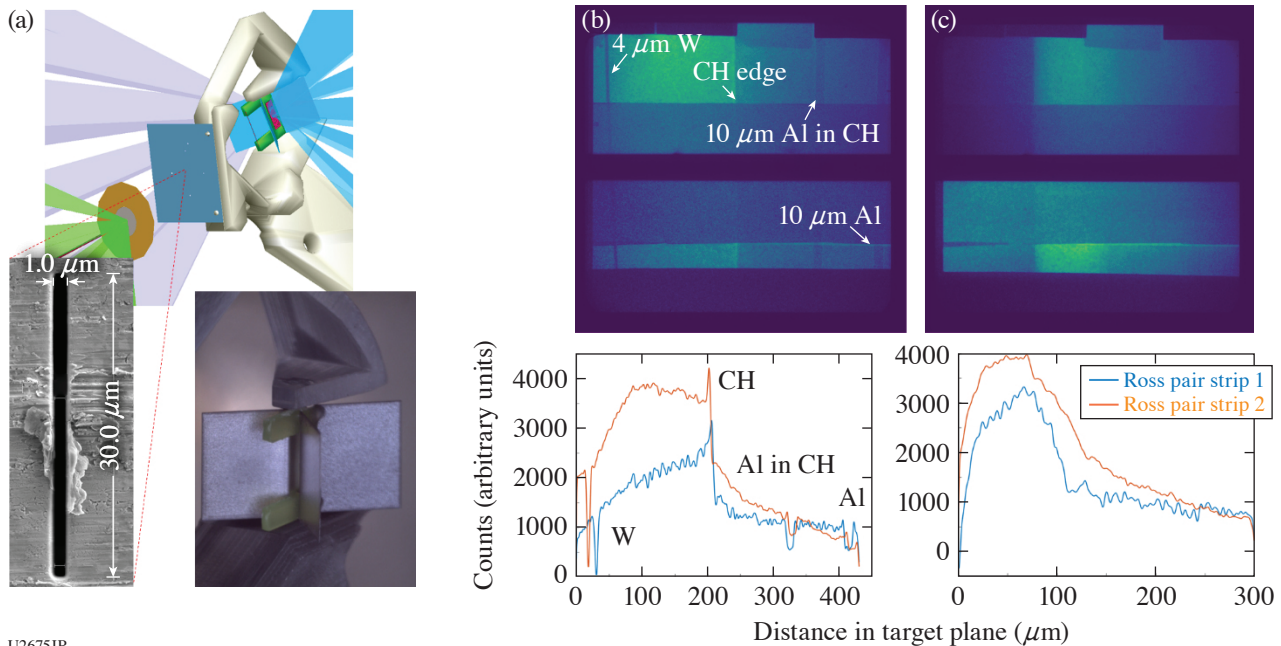


Figure 4

(a) Driven target configuration in a monolithic frame. The two detailed images are (left) a SEM image of a $1\text{-}\mu\text{m}$ -wide slit and (right) the driven target in the frame. (b) Radiographs and lineouts from a cold wire target, showing features from a variety of wires including strong refraction contrast at the CH surface. (c) Radiographs and lineouts of a driven target. The change of the CH signal across the strips is the rarefaction wave from expansion and can be used to calibrate the x-ray drive by comparing to simulation.

Viscosity Measurements Using Tracer Particles

Principal Investigators: A. E. Gleason (SLAC); D. N. Polsin, J. J. Ruby,* R. Rygg,*† G. W. Collins,*† P. M. Nilson, and R. Betti*† (LLE); and J. K. Shang, H. A. Aluie, N. Acharya, and D. H. Kelley (Dept. of Mechanical Engineering, University of Rochester)

*Also Dept. of Physics and Astronomy, University of Rochester

†Also Dept. of Mechanical Engineering, University of Rochester

Viscosity has an important role in the evolution of hydrodynamic instabilities and the mixing between materials, especially at early times at scales smaller than of the order of $100\ \mu\text{m}$ (Refs. 9 and 10). Our objective was to measure viscosity in a hydrocar-

bon plastic (CH) at HED conditions, which is commonly employed in target fabrication for ICF and basic science experiments. In this experiment, we shock compressed the CH and imaged the deformation and movement of small, high-Z particles embedded in the target over time. The viscosity plays a role in how well a particle tracks the surrounding fluid and can be inferred by comparing trajectories of particles of different sizes and/or densities after a shock has passed. The experiment was a continuation of the pilot FY19 campaign and is part of a broader effort to develop an x-ray particle image velocimetry (XPV) platform as a technique to measure more-complex flows.

Experimental Configuration

The target bulk was composed of particle-seeded epoxy (Stycast 1266, 1.12 g/cm^3). Layers of epoxy were drilled with small holes at the desired positions in which the high-Z particles were placed, backfilled, and assembled with adhesive. Each target contained three particle pairs, where each pair consisted of a large ($60\text{-}\mu\text{m}$) and small (40- or $50\text{-}\mu\text{m}$) spherical particle aligned collinearly center-to-center, such that the impinging shock should pass through the center of both particles approximately simultaneously. Particles were Ti or stainless steel (Cospheric). Particle pairs were $100 \mu\text{m}$ apart. A Kapton ablator and Au heat shield were placed on the drive side of the target. Targets were fabricated by Gryphon Technologies.

Drive beams (0.8 kJ , 7.4 ns) irradiated the Kapton ablator at the front of the target using $760\text{-}\mu\text{m}$ distributed phase plates, driving a shock through the target. Additional beams irradiated a copper backlighter with a 1-ns square pulse; a pinhole array ($20 \mu\text{m}$) and a gated x-ray framing camera were positioned on the P6–P7 axis opposite the backlighter [Fig. 5(a)]. Framing-camera strip-time delays were varied to obtain particle-shock interactions at different times. The 0.1-ns gate duration of the framing camera provided sufficient temporal resolution to locate the particle locations, with 20-km/s particle speeds (estimated from hydrodynamics simulations with *FLASH*) blurring location by only $2 \mu\text{m}$. Shock speeds as a function of time were measured by VISAR (velocity interferometer system for any reflector).

Results

Particles were clearly imaged with area backlighting at various times during target compression, as shown in Fig. 5(b). The shock interface and deformation of the shocked particles were evident and agree well with a previous experiment at NOVA conducted by Klein *et al.*¹¹ As part of this campaign, our team is concurrently developing a method to approximate the deformation resistance of the solid particles at early times with a modified ideal-gas equation of state in radiation-hydrodynamics code (*FLASH*). In Fig. 5(b), we show that particle shapes simulated by this equation-of-state (EOS) method agree well with the

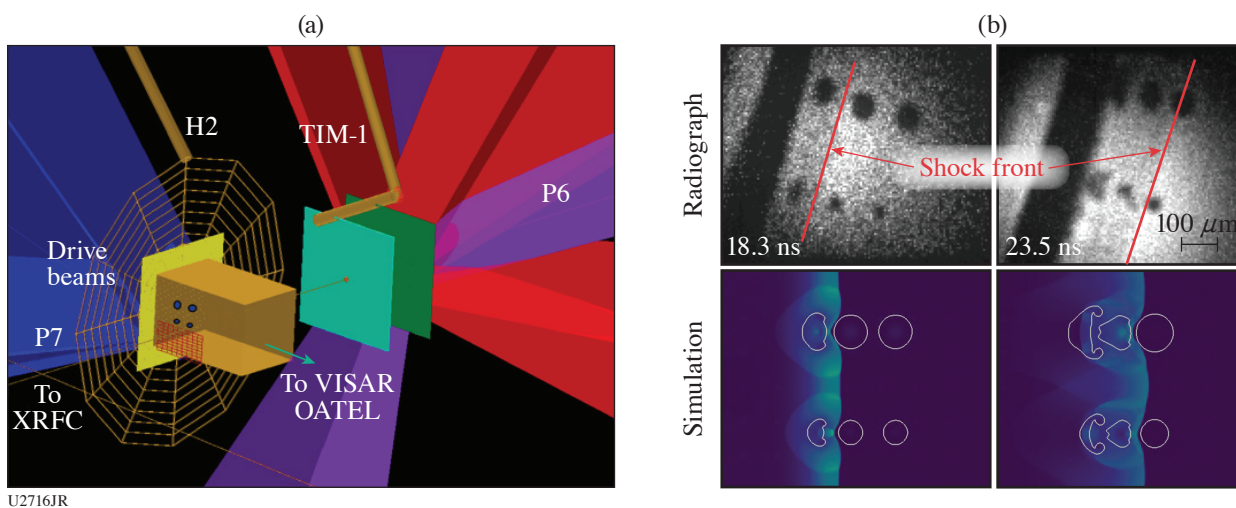


Figure 5

(a) Target configuration. (b) Stainless-steel particles at two times during CH target compression, obtained with an x-ray framing camera on OMEGA (Sept. 2020). The particle deformation (dark bodies, top) agrees well with *FLASH* simulations (particle outlines shown in white, bottom).

experimental images. Excellent VISAR data were obtained, and the timing of the radiography data will be correlated with the measured shock velocity. We estimate that a 480-GPa shock front in epoxy was achieved.

Image analysis to determine particle displacement is in progress.

Dissemination, Training, and Professional Development

Results related to this effort were presented at the 2020 Stewardship Science Academic Programs (SSAP) Symposium (February 2020) and Division of Plasma Physics Meeting (November 2020) by senior personnel and graduate students.

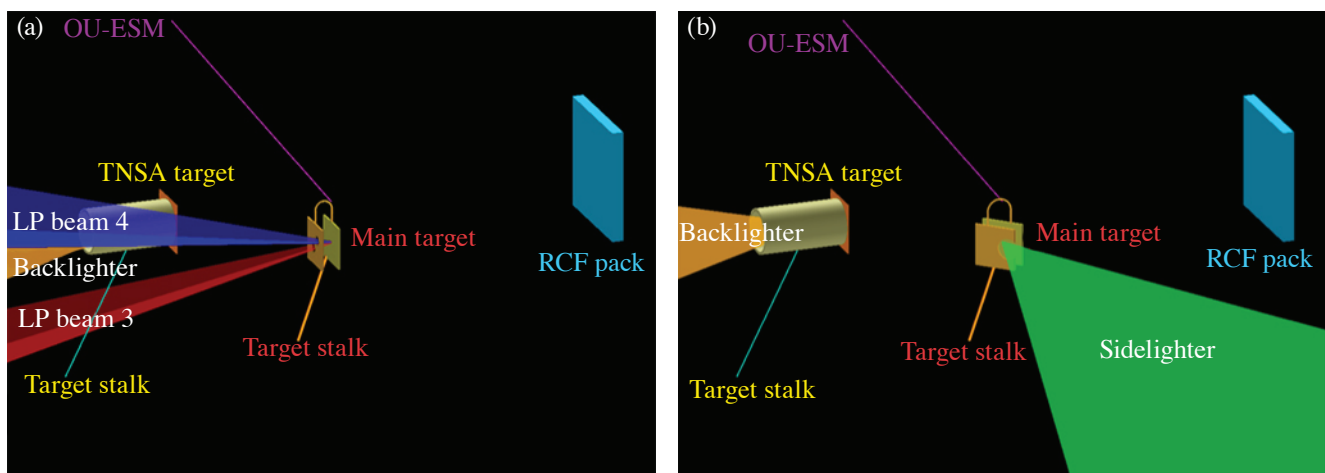
This work was performed under the auspices of the U.S. Department of Energy and NNSA under Grant DE-SC0019329 within the joint HEDLP program and the Stewardship Science Academic Alliances under Grant DE-NA003914.

LBS Campaign FY20—Magnetic-Field Generation with Laser-Powered Capacitor Coils

Principal Investigators: H. Ji, L. Gao, A. Chien, and S. Zhang (PPPL); E. G. Blackman (Dept. of Physics and Astronomy, University of Rochester); P. M. Nilson (LLE); G. Fiksel (University of Michigan); and H. Chen (LLNL)

The LBS Campaign in FY20 focused on two main goals: (1) to optimize laser-powered capacitor coils¹² as an external magnetic-field source generator and (2) to build a comprehensive lumped-circuit model for the capacitor coil platform, including important physics processes such as the laser–solid interaction, plasma effects, and electron distribution.

These goals were achieved in two major laser-drive regimes: UV long-pulse drive and IR short-pulse drive. In the UV case, the capacitor-coil target is driven by OMEGA EP Beamlines 3 and 4, while in the IR case, Beamline 1 in sidelighter mode is used to energize the target. In both cases, the capacitor-coil design consists of two parallel copper plates connected by a thin copper wire folded into a U-shaped coil. Experimental setups for UV and IR drives are shown in Figs. 6(a) and 6(b), respectively. Hot electrons are generated as the laser beam hits the back plate, building up a voltage difference between the plates and driving a large current through the connecting coil. This results in strong magnetic-field generation around the coil. The magnetic-field strength and coil current are inferred using TNSA (target normal sheath acceleration) proton radiography: measurement of the prolate void feature generated by the magnetic-field structure can be compared with synthetic radiographs from ray tracing.



U2717JR

Figure 6

(a) OMEGA EP experimental setup for long-pulse drive of the capacitor coil. Beamlines 3 and 4 drive the main target, and the coil magnetic fields are diagnosed with TNSA protons driven by the backlighter. (b) OMEGA EP experimental setup for short-pulse drive of the capacitor coil. The sidelighter beam drives the main target at a 45° incidence angle, and the coil magnetic fields are diagnosed with TNSA proton radiography.

In UV drive, a fixed intensity of 1.7×10^{16} W/cm² was used for all shots. A laser pulse duration scan was conducted with square pulse widths of $t_L = 2, 3, 4,$ and 9.9 ns. Accounting for proton time-of-flight from the TNSA interaction, the radiographs represent field measurements taken at roughly the end of the square laser pulse. Prolate voids of varying sizes were formed for all long-pulse shots (Fig. 7). Comparing the voids with synthetic radiographs, coil currents were inferred for the laser pulse widths to be $17 \pm 1, 13 \pm 1, 11 \pm 1,$ and 10 ± 1 kA for pulse widths of 2, 3, 4, and 9.9 ns, respectively. A clear decreasing trend is established in generated coil current with increasing laser pulse duration at constant intensity.

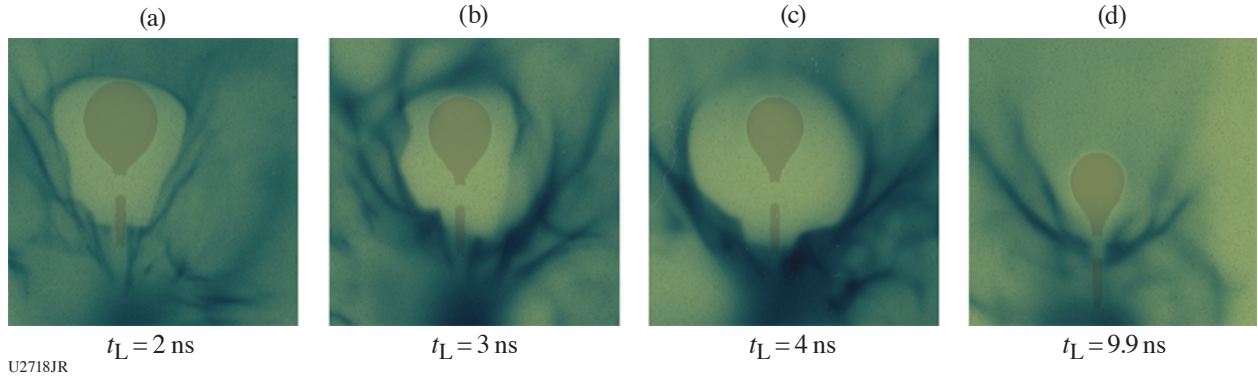


Figure 7

Experimental proton radiographs for laser pulse widths of (a) 2, (b) 3, (c) 4, and (d) 9.9 ns. Laser intensity is the same for all shots at 1.7×10^{16} W/cm². The experimental data are overlaid with synthetic radiographs of coil-generated magnetic fields, corresponding to inferred currents of $\pm 17, \pm 13, \pm 11,$ and ± 10 kA, respectively. The overlays indicate close agreement in structure and size of the primary feature.

A lumped circuit model¹³ was developed to characterize the effects of an intense laser pulse on such a capacitor-coil target. The current through the coil is modeled by characterizing the target as an RLC series circuit. Voltage between the plates, U , is described by a combination of ion and electron currents, as well as the coil current. The electron current can be described as the sum of two Boltzmann distributions at different temperatures. The ion current is assumed to follow a self-similar expansion model. Combining the expressions for the current sources and including the other components of the RLC circuit to describe the behavior of the voltage between the plates, the model becomes a set of coupled differential equations:

$$C \frac{dU}{dt} \begin{cases} I_{i0} \exp(-d/c_s t) - K_h I_{e0} \exp(U/T_{e,h}) - (1 - K_h) I_{e0} \exp(U/T_{e,c}) + I_c & 0 < t \leq \tau_1 \\ I_{i0} \exp(-d/c_s t) \exp[-(t - \tau_1)/\tau_{d,i}] - [K_h I_{e0} \exp(U/T_{e,h}) + (1 - K_h) I_{e0} \exp(U/T_{e,c})] \exp[-(t - \tau_1)/\tau_{d,e}] + I_c & t > \tau_1 \end{cases}$$

$$-U = RI_c + L \frac{dI_c}{dt}.$$

The lumped-circuit model indicates a rise and subsequent saturation of coil current with increasing laser pulse duration. By varying the model, it can be seen that this is due to the arrival of ions reaching the front plate, which effectively “shorts” out the circuit. The phenomenon occurs on a time scale similar to the ion transit time $\tau_i \sim d/c_s$. A comparison of experimental data and the lumped-circuit model is shown in Fig. 8.

The short-pulse-drive experiments were conducted at varying intensities and pulse widths. The varied parameters allow us to build a comprehensive “phase diagram” of achievable currents and magnetic fields based on the laser parameters of intensity and pulse width. At constant laser pulse width of 5 ps, a laser intensity scan was performed, ranging from 2.8×10^{18} W/cm² to 2.0×10^{19} W/cm². On the other axis, a pulse width scan was performed at a constant intensity of 2.8×10^{18} W/cm², ranging from 5 ps to 50 ps. Additionally, a maximum intensity shot of 6.7×10^{19} W/cm² was performed, using 300 J over 0.7 ps.

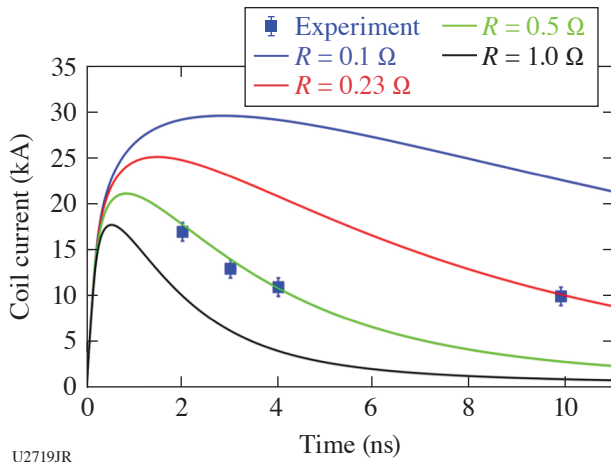


Figure 8
Lumped-circuit model simulations of coil current as a function of laser pulse duration, compared with experimental measurements. In the model, resistance is assumed constant for each run, but varied as a free parameter to account for temperature effects. $R = 0.5 \Omega$ provides the best match to experimental measurements but diverges at late time. $R = 0.23 \Omega$ matches the data point at $t = 9.9$ ns. In all cases, coil current is observed to eventually decay with increasing laser pulse width due to ion shorting.

Data analysis is ongoing, but preliminary results demonstrate great promise for short-pulse-driven capacitor coils as a platform for external magnetic field generation. TNSA proton radiographs for an intensity scan at constant laser energy are shown in Fig. 9. The radiographs demonstrate coil currents of 90 ± 10 , 85 ± 10 , and 75 ± 10 kA for laser pulse widths of 100 ps, 50 ps, and 15 ps, respectively. For all shots, laser energy on target was 1 kJ. Despite the lower energy on target than the long-pulse drivers, higher coil currents were achieved. This represents a conversion efficiency of up to $11\times$ larger than achievable with the long-pulse drive on OMEGA EP. With further data analysis, we hope to gain insight into hot-electron physics, as well as the mechanisms behind current generation to produce a self-consistent lumped-circuit model for short-pulse-driven capacitor coils.

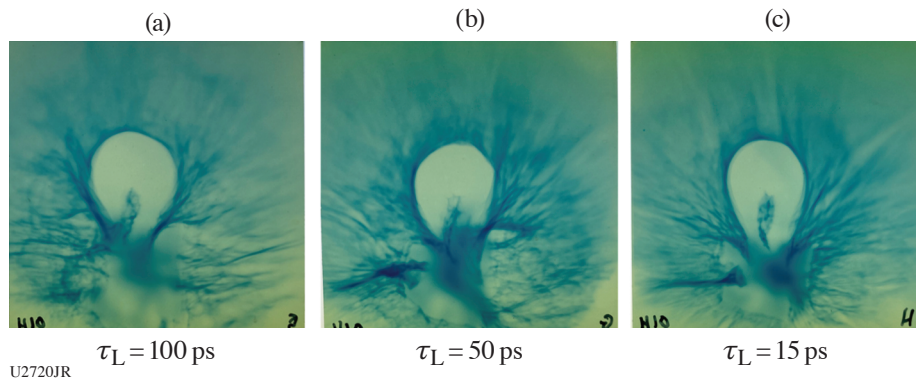


Figure 9
(a) 100-ps, (b) 50-ps, and (c) 15-ps pulse widths. Proton radiographs of the magnetic field generated by a short-pulse-driven interaction for various pulse widths. For all shots, laser energy on target was 1 kJ at best focus. The radiographs represent coil currents of 90 ± 10 , 85 ± 10 , and 75 ± 10 kA, respectively.

This material is based upon work supported by the Department of Energy National Nuclear Security Administration under LBS Award Number L2034.

Characterizing Pressure Ionization in High-Density Mid-Z Materials with X-Ray Fluorescence Spectroscopy

Principal Investigators: S. Jiang, Y. Ping, A. Lazicki Jenei, P. Sterne, P. Grabowski, H. Scott, R. Smith, R. Shepherd, B. Bachmann, and J. H. Eggert (LLNL); and S. B. Hansen (SNL)

This campaign comprised one day on OMEGA EP during FY20. In our previous campaigns, we had for the first time provided a direct benchmark between various isolated-atom and average-atom ionization models by measuring K-shell emission of Co. During the FY20 campaign, we have extended the method to L-shell emissions of mid-Z materials Tb and Dy.

A schematic of the experimental setup is displayed in Fig. 10(a). The fluorescence line emissions were induced by hot electrons generated through short-pulse, laser–solid interactions. A large, thick Al target was used to avoid heating from the short pulse. The high pressure was achieved by ramp compression using the long-pulse drivers, so that the temperature was kept low during the compression process. During the experiment, the pressure history was characterized with VISAR measurements. We have varied the driver energies to reach different densities. The target structure is also shown in Fig. 10(a). Despite the Tb or Dy layer under study, we have also included a thin Co layer as an energy reference. The main diagnostic used in this campaign was a high-resolution imaging x-ray Thomson spectrometer (IXTS) with a user-provided Ge crystal to accommodate the required energy range.

We have successfully measured the Co K_{α} fluorescence line and multiple Tb/Dy L_{β} lines with high signal-to-noise ratio as can be seen in Fig. 10(b). According to our previous Co study, the Co K_{α} line has negligible energy shift under the designed experimental conditions since the inner K, L shells are not greatly affected by pressure ionization; therefore, the measured spectra under various conditions can be aligned with the Co K_{α} peak. The M, N shells that are responsible for the multiple L_{β} emissions of Tb and Dy are much more prone to both the ionization pressure depression effect and the density-dependent plasma polarization effect. Under maximum compression, we have observed a +1-eV blue shift in Tb $L_{\beta 1}$, a -3-eV red shift in Tb $L_{\beta 2}$, and no shift in Tb $L_{\beta 3}$. For Dy, a small +1-eV blue shift was observed in both its $L_{\beta 1}$ and $L_{\beta 3}$. While further analysis is still in progress, we have seen evidence of various competing effects in the measured line shifts, which can be used to directly benchmark various ionization models for mid-Z materials.

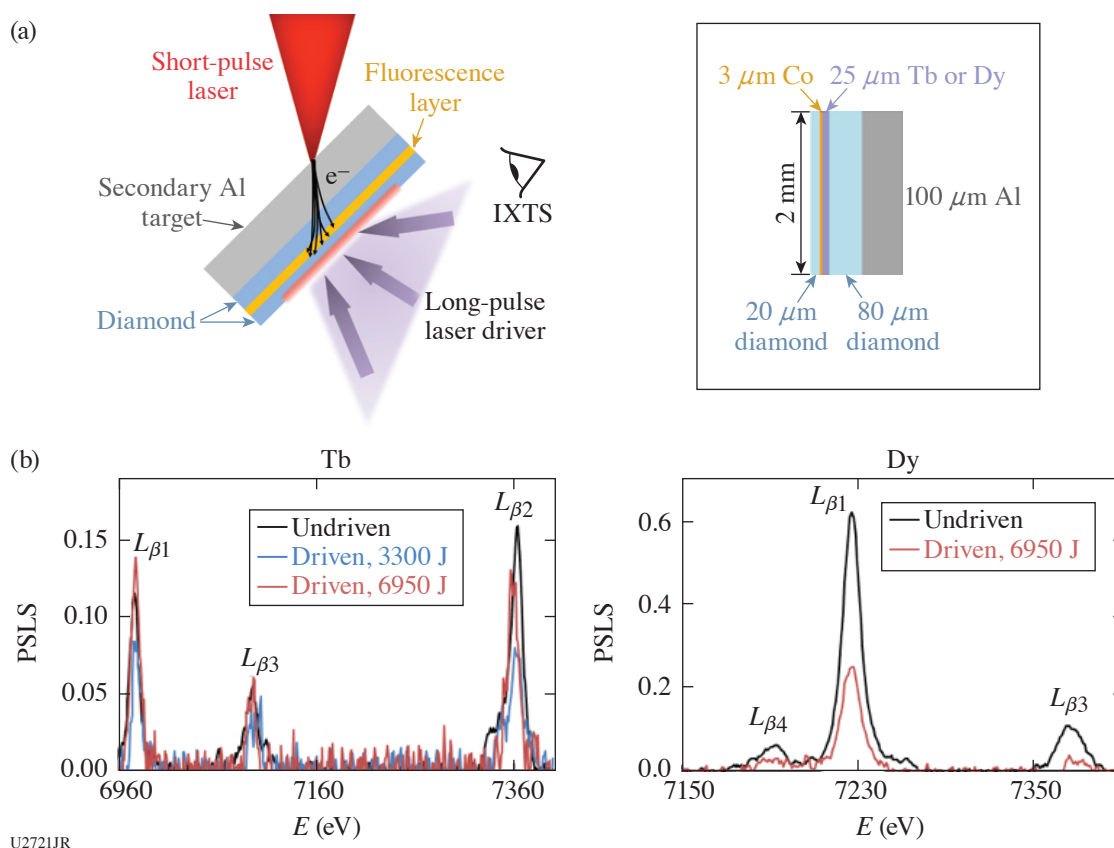


Figure 10

(a) A schematic diagram of the experimental configuration. (b) Measured IXTS spectra of Tb and Dy L-line emissions. The spectra under different conditions are aligned with the Co K_{α} emission line.

Measurements of Shock Equation of State and Melting Temperature on Water–Ammonia Mixtures

Principal Investigators: Y.-J. Kim, S. Hamel, and M. Millot (LLNL); M. Bethkenhagen (Rostock University, Germany); M. Wadas (University of Michigan); and S. Stanley (Johns Hopkins University)

This SuperionicMix-20 Campaign aims at investigating the optical and thermodynamic properties of water–ammonia mixtures at the extreme pressure–temperature conditions that we expect in the deep interior of icy giant planets such as Uranus and Neptune. This work at the Omega Laser Facility expands on our recent discovery of superionic water ice (or ice XVIII)^{14,15} to reveal the possible existence of the superionic phase in the icy planet constituents (H:C:N:O) as well as its melting temperature.

We used a diamond-anvil cell (DAC) to increase the initial sample density at room temperature, achieve lower temperatures but higher compression under dynamic loading, and finally reach planetary interior conditions. With excellent laser performance and support, we collected 14 system shots in the two half-day allocations. Doppler velocimetry (VISAR) [Figs. 11(a) and 11(b)] and streaked optical pyrometry (SOP) [Fig. 11(c)] were used to track the shock-wave propagation through the precompressed sample and to document the pressure–density–temperature shock equation of state as well as the evolution of the optical properties (reflectivity and absorption coefficient) along the shock Hugoniot curves using quartz.¹⁶

The ongoing data analysis will be used to improve our understanding of how the icy planet constituent of H:C:N:O mixtures behave at the extreme pressure–temperature condition inside the planets.

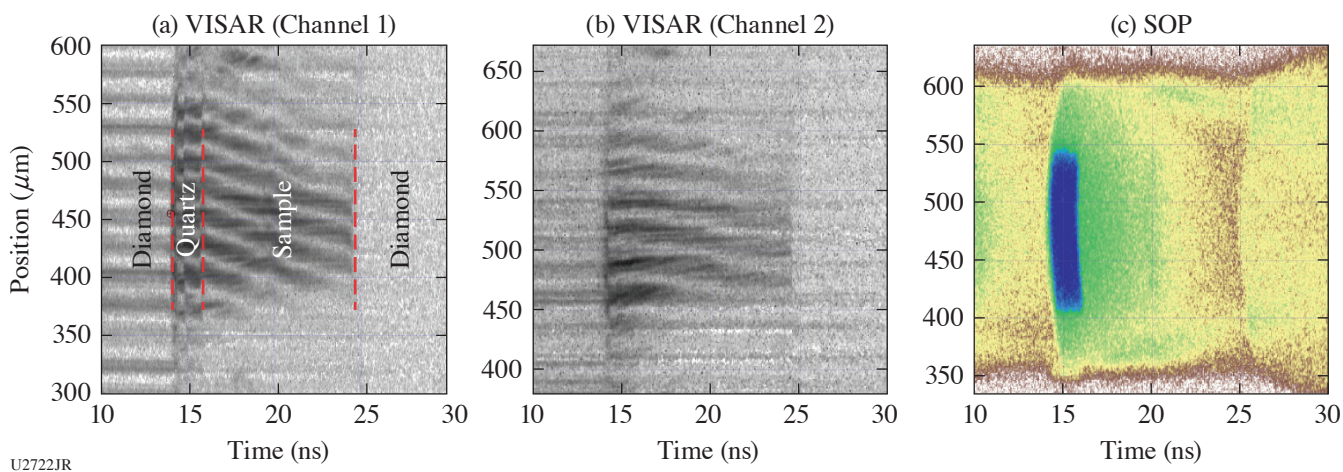


Figure 11
Examples of [(a),(b)] VISAR and (c) SOP data showing the decaying shock along the 150- μm -thick water–ammonia mixture on OMEGA 60.

Experimental Study of the Dynamics of Expanding Magnetized Laser-Produced Plasma

Principal Investigators: S. Malko,^{*} W. Fox,[†] and A. Bhattacharjee[†] (PPPL); D. B. Schaeffer and A. Spitkovsky (Princeton University); C. Johnson (Rowan University); G. Fiksel (University of Michigan); P. Knapp (SNL); A. Ciardi (Observatoire de Paris, Sorbonne Université and CNRS, France); and J. R. Davies (LLE)

^{*}Also Centro de Laseres Pulsados, Spain

[†]Also Princeton University

The interaction of an expanding plasma with a magnetic field plays a key role in magnetized fusion schemes such as magnetized liner inertial fusion (MagLIF),¹⁷ laboratory astrophysics experiments such as magnetic reconnection¹⁸ and magnetized collisionless shocks,¹⁹ and space-plasma experiments such as Active Magnetospheric Particle Tracer Explorers.²⁰

These topics motivate an understanding of magnetic-field transport properties in laser-produced HED; another aspect of interest is anomalous fast diffusion of plasma caused by strong plasma gradients, causing particles and field to mix and diffuse with respect to one another. These processes can determine the time and space scales over which plasma heat can be effectively confined by the magnetic field. Under certain conditions, the magnetic-field diffusion is enhanced by plasma instabilities, of either the lower-hybrid type, which have a short wavelength and result from the coupling of gradient-driven modes to the lower-hybrid range modes $\omega \sim \omega_{\text{LH}} = (\omega_{\text{ce}}\omega_{\text{ci}})^{1/2}$, or the large-Larmor-radius Raleigh–Taylor (RT) instabilities, in which the magnetic field acts like a “light fluid” to decelerate an expanding “heavy” plasma (by its pressure force). Such instabilities may also be present in the MagLIF scheme, and by scaling using dimensionless parameters,²¹ we can study a set of common physics at smaller-scale facilities. Here we report on an experiment on OMEGA that focused on the study of the magnetic-field dynamics in HED plasma in a relevant regime ($\beta > 1$), covering the magnetic-field evolution time along with its diffusion and potential anomalous transport processes.

The schematic experimental setup on OMEGA is shown in Fig. 12. The magnetized laser-produced plasma is generated by ablating a CH plasma into a quasi-static magnetic field produced by the MIFEDS pulsed-power system. The evolution of the 2-D global topology of the magnetic fields was imaged with proton radiography by 3-MeV and 15-MeV protons, acquired at different plasma expansion times. A novel technique of the proton radiography was developed to obtain an absolute reference of undeflected beamlets for each shot. The corresponding local plasma parameters—electron temperature and density—were measured with 2ω Thomson scattering.

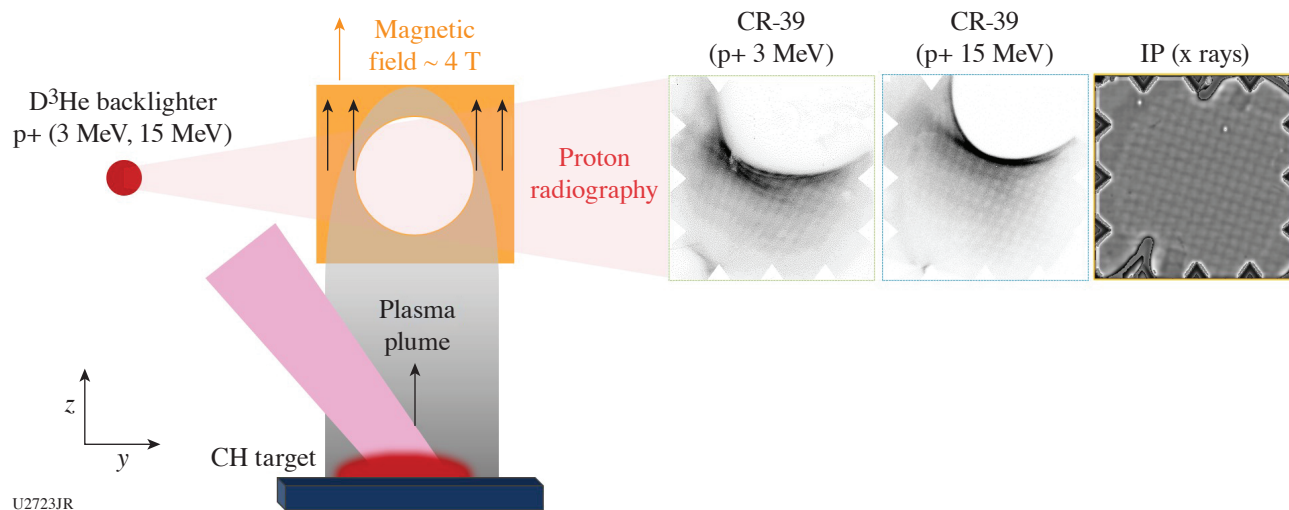


Figure 12

Schematic of the experimental setup showing the raw images obtained with a novel proton radiography technique. The CR-39 stack was composed of CR-39 for 3-MeV and 15-MeV protons and an image plate (IP) in the back of the stack for an x-ray image of the nickel mesh.

The magnetic-field dynamics in plasma has been explored for different laser energies and target orientations relative to field. Here we show the preliminary experimental results for one of the experimental configurations as shown in Fig. 12. In the experiment we observe the expanding plasma expelling the magnetic field out of its volume and forming a diamagnetic cavity. A clear magnetic-field temporal evolution in plasma can be seen in Fig. 13(a), which shows the path-integrated magnetic field $\int B dl$ at different plasma expansion times, compared to the vacuum magnetic-field profile with no plasma, as calculated by a COMSOL model of the MIFEDS coil windings. The magnetic field is observed to be mostly expelled by the plasma between 20 ns (red curve) and 30 ns (green curve) and then gradually returns. The experimental radii of the diamagnetic cavity are estimated by fitting data with the synthetic magnetic field with artificial cavities of various sizes. These are compared with the radii obtained from *GORGON* 3-D magnetohydrodynamic (MHD) simulations in Fig. 13(b). *GORGON* 3-D MHD simulations were employed to qualitatively observe the effect in similar conditions. The preliminary analysis shows a rapid diamagnetic expansion followed by collapse, in qualitative agreement with *GORGON* 3-D MHD simulations.

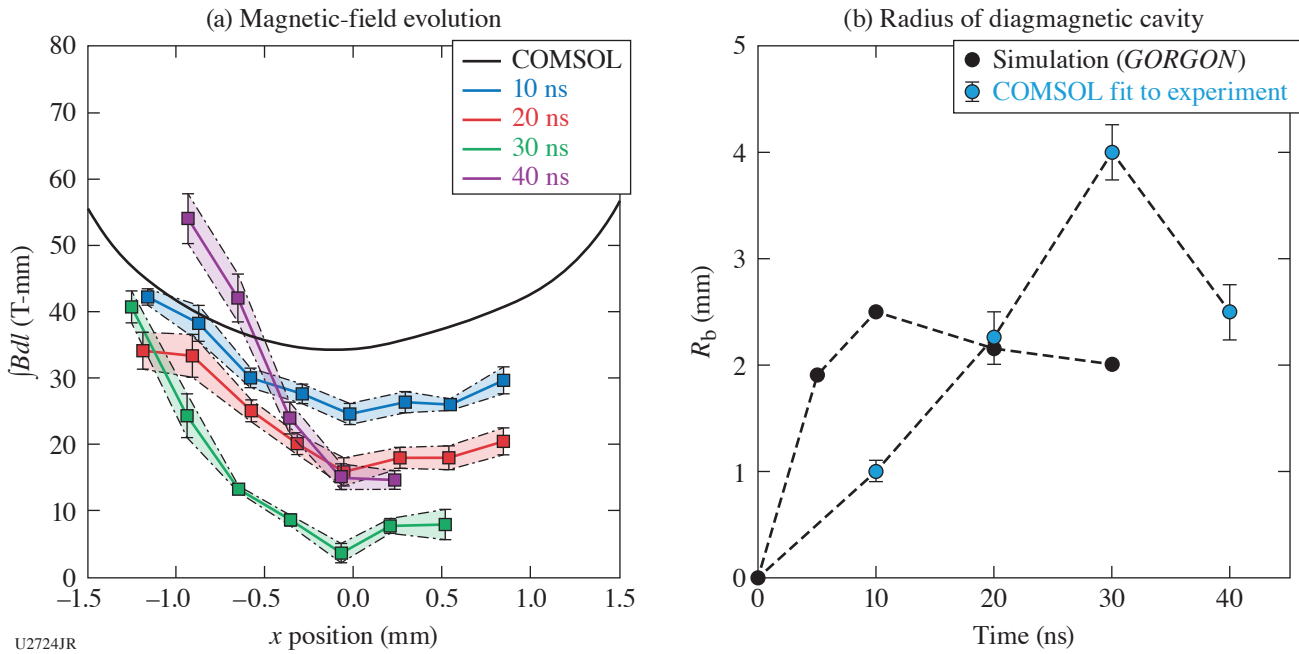


Figure 13

(a) The path-integrated magnetic field at each expansion time. (b) The radius of the diamagnetic cavity at each expansion time obtained in experiment (blue circles) and in *GORGON* 3-D MHD simulations (black circles).

In summary, we have developed a novel technique of proton radiography with a reference x-ray image of the mesh for precise measurement of the magnetic field. Using this method, we have performed a characterization of the diamagnetic cavity formation and time evolution in $\beta > 1$ expanding plasma. The results, which were compared to the simulated magnetic-field dynamics in similar conditions with *GORGON* 3-D MHD, suggested a faster diffusion than predicted classically of $1 \mu\text{s}$.

Measurements of the DT and DD Neutron Energy Spectrum in High-Temperature Plasmas

Principal Investigators: O. M. Mannion, C. J. Forrest, V. Yu. Glebov, J. P. Knauer, P. W. McKenty, Z. L. Mohamed, S. P. Regan, and C. Stoeckl (LLE); P. Adrian, J. A. Frenje, M. Gatu Johnson, and N. Kabadi (Plasma Science and Fusion Center, MIT); B. D. Appelbe and A. J. Crilly (Imperial College London, UK); and W. Taitano (LANL)

The goal of ICF experiments is to generate a hot dense thermonuclear plasma that releases more energy from thermonuclear fusion than was required to initially assemble the plasma. A key parameter required to understand the performance of these experiments is the temperature of the hot fusing plasma. Traditionally, the temperature of the hot fusing plasma is determined from measuring the variance (second moment) of the DT and DD neutron energy spectra emitted from the target. The second moment of the neutron energy spectrum is altered if nonthermal motion of the fusing plasma exists within the hot spot and can result in the inferred temperature being higher than the true thermal temperature. Therefore, alternative techniques to infer the hot-spot temperature, such as electron-ion temperature measurements, are being pursued in the ICF community.

Motivated by this pursuit, we have executed a set of experiments that investigated a new method to infer the thermal ion temperature. In this method the Gamow velocity shift (first moment) of the neutron spectrum emitted from the hot fusing plasma²² is used to infer the plasma ion temperature. The Gamow velocity shift is not susceptible to nonthermal motion of the hot spot like the second moment is, so provides an alternative and robust method to infer the temperature of the plasma. In this work we have experimentally demonstrated this technique and have inferred the ion temperature from the Gamow velocity shift for plasmas between 2 to 18 keV. We found that good agreement exists between the first- and second-moment temperatures until the Knudsen number^{23,24} ($K_n = \lambda_{ii}/L$) approaches unity. For a Knudsen number that exceeds unity we see discrepancies between the two different temperature measurements, which is likely a sign that the ion velocity distribution within the fusing plasma is non-Maxwellian.

The goal of this work was to compare the first- and second-moment ion temperatures over a large range of ion temperatures. Therefore, a series of thin glass DT-filled targets were imploded on OMEGA using 1-ns and 600-ps square pulses with fill pressures of 5 and 10 atm. In these implosions a strong shock that is sent through the fuel heats the DT fuel. By varying the laser energy and fill pressure, ion temperatures were varied between 2 to 18 keV. The DT and DD neutron energy spectra produced from these plasmas were then measured using a suite of neutron time-of-flight (nTOF) detectors, and the first and second moments were inferred. A semi-relativistic neutron spectrum model²² was used to infer the plasma ion temperature from the first and second moments independently.

In these high-temperature experiments, kinetic effects have been observed in past experiments, indicating that the ion velocity distribution may not be Maxwellian in these plasmas. Therefore, a suite of secondary diagnostics were used to fully characterize the hot plasma conditions. This included charged-particle spectrometers such as the magnetic recoil spectrometer (MRS) and the charged-particle spectrometer (CPS), which measured the knock of the deuteron spectrum and were used to infer the hot spot's areal density. The proton core imaging spectrometer diagnostic was run in x-ray imager mode and measured the morphology of the hot spot at different photon energies, which enable us to infer the hot-spot radius and the electron temperature. Finally, the neutron temporal diagnostic was used to measure the fusion reaction history. Using all of these measurements, along with the ion temperatures measured using the nTOF's, the ion mean free paths in these experiments were determined. Finally, using the ion mean free path and hot-spot radius measurements, the plasma Knudsen number was inferred.

The ion temperatures inferred from the first and second moments are shown in Fig. 14 for both the DT and DD neutron spectra. Good agreement is observed between the inferred ion temperatures for all but the high-ion-temperature cases. In these high-temperature experiments, the Knudsen number exceeded unity as indicated in Fig. 15, which shows the ratio of the first- and second-moment inferred ion temperatures as a function of the Knudsen number. It is observed that for Knudsen numbers below 1, there is good agreement between the temperatures inferred using both methods. As the Knudsen number exceeds unity, a discrepancy is observed. In particular for the DT spectrum's inferred temperature, the first-moment temperature appears to plateau, while the second-moment ion temperature continues to increase (see Fig. 14). Conversely for the DD inferred temperatures, the second-moment inferred ion temperature appears to plateau at high Knudsen number, while the first-moment inferred ion temperature continues to increase (see Fig. 14).

These experiments are currently being simulated using a Vlasov–Fokker–Plank (VFP) code²⁵ developed at LANL, which should accurately capture the non-Maxwellian nature of these shock-drive implosions. A fully kinetic neutron spectrum calculation

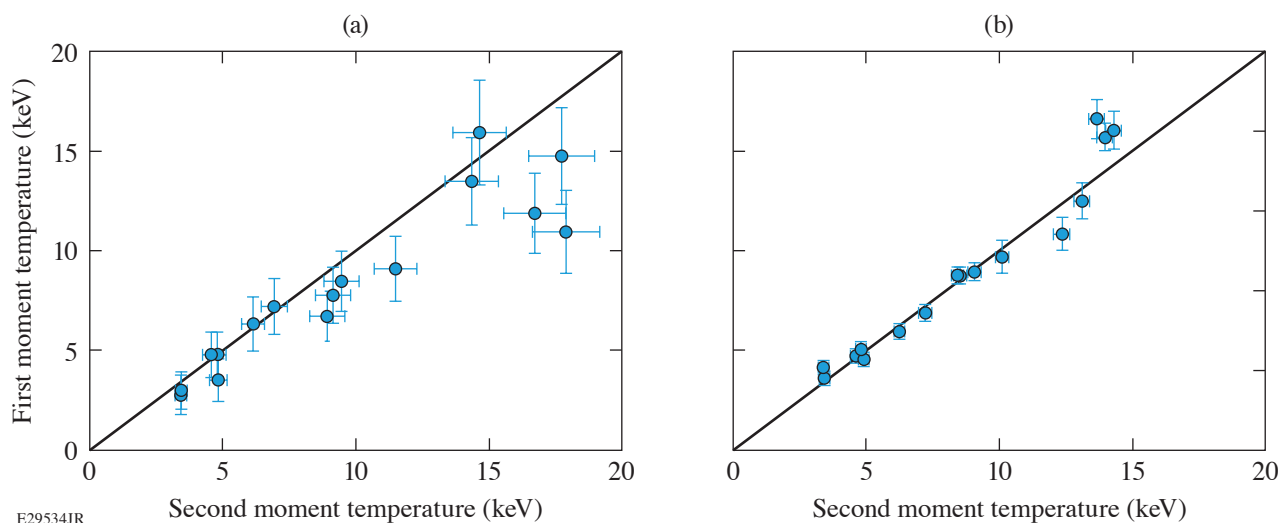


Figure 14

The inferred ion temperature from the first moment of the neutron spectrum as a function of the second moment of the neutron spectrum for the (a) DT and (b) DD neutron energy spectra.

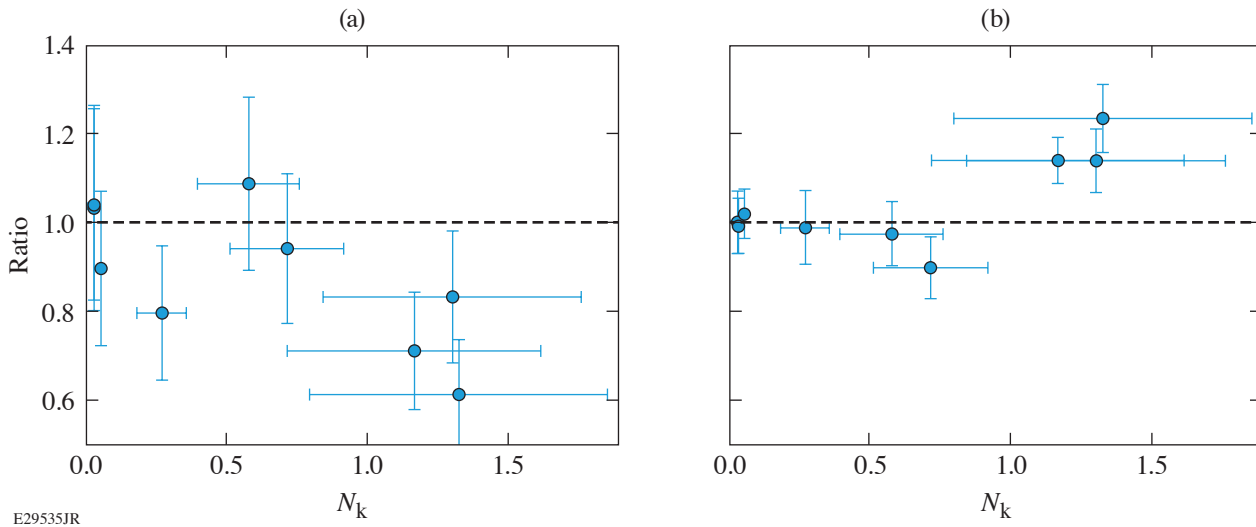


Figure 15

The ratio of the inferred ion temperature from the first and second moments of the (a) DT and (b) DD neutron energy spectra as a function of the Knudsen number.

package has been developed to post-process the VFP simulation results and will be used to study the effect of non-Maxwellian distributions on the neutron energy spectrum. These experimental results will be used as key benchmarks of these fully kinetic simulations and will provide insights into the physics occurring in high-temperature fusing plasmas.

This material is based upon work supported by the Department of Energy National Nuclear Security Administration under Award Number DE-NA0003856, the University of Rochester, and the New York State Energy Research and Development Authority.

Extreme Atomic Physics: Changes in the Electronic Structure of Compressed Materials

Principal Investigators: P. M. Nilson and S. X. Hu (LLE); and S. B. Hansen (SNL)

Understanding how atomic physics may be altered in HED conditions is important to the study of stellar interiors, planetary cores, and inertial fusion. Warm dense matter is just one type of system that is intrinsically challenging because the system's thermal energy, Fermi energy, and Coulomb energy are all comparable, thereby causing traditional plasma approximations to no longer be valid. The goal of this campaign is to test the atomic-scale models that are used to estimate changes in the electronic structure of compressed materials and understand how atomic physics may be altered in these conditions.

To measure detailed x-ray spectroscopic features from dense, high-temperature matter, a self-backlit, spherical-implosion platform is being developed on the OMEGA Laser System. The target design uses a spherical shell with a CH ablator, a central CH layer doped with 4 at. % Cu, and an inner CH layer. The target contains a 20-atm D₂Ar (1 at. %) fill and is assembled by direct laser ablation using a 27-kJ, 1-ns drive. Continuum emission generated in the core at bang time backlights the assembled shell. By actively manipulating the sample compression and heating, experiments are underway to study how the K-shell emission and absorption are altered in the imploding Cu-doped layer.

Figure 16 shows time-integrated x-ray emission and absorption spectra from two different targets. Figure 16(a) shows data from a 30- μ m-thick shell containing a 10- μ m CHCu (4 at. %) layer and a 3- μ m inner CH layer. The measured spectrum shows the Cu K-shell emission and resonant self-absorption. Figure 16(b) shows data from a 30- μ m-thick shell containing a 5- μ m CHCu (4 at. %) layer and a 10- μ m inner CH layer. The thicker inner layer protects the compressed Cu-doped layer from core heating, showing a clear absence of $1s-2p$ absorption. In addition to the development of high-resolution x-ray imaging of the buried layer, analyses of simultaneous time-integrated and time-resolved x-ray emission and absorption spectra are underway for comparison with model predictions. These data will be used to test modern density functional theory calculations and the atomic-scale models that are used to estimate changes in the electronic structure of highly compressed materials.

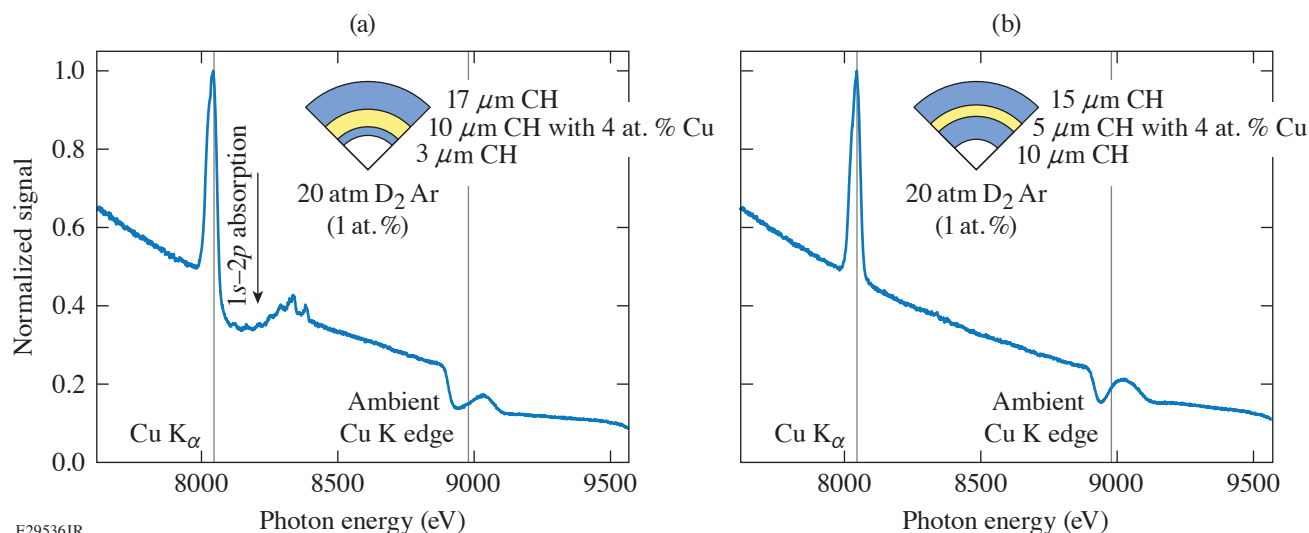


Figure 16

Example time-integrated x-ray absorption features and fluorescent line emission from a laser-driven implosion containing a Cu-doped layer. The target designs are shown in the insets.

This material is based upon work supported by the Department of Energy National Nuclear Security Administration under Award Number DE-NA0003856, the University of Rochester, and the New York State Energy Research and Development Authority.

Development of a New Experimental Platform LIANS on OMEGA EP for Deuteron- and Triton-Induced Nuclear Reactions

Principal Investigators: A. K. Schwemlein,* C. Stoeckl, W. T. Shmayda, and W. U. Schröder* (LLE)

*Also Dept. of Physics and Astronomy, University of Rochester

The OMEGA EP Laser System was used to create a deuteron beam through TNSA with deuterated metal foils at intensities close to 10^{19} W/cm². In previous experiments, deuteron beams were generated with this mechanism using either plastic²⁶ or heavy water^{27,28} targets. Deuterium-doped titanium substrates were extensively studied²⁹ previously on the Multi-Terawatt (MTW) laser to produce a controllable deuterium beam with yields exceeding 10^{11} deuterons per shot. Separate studies using deuterated plastic targets demonstrated the feasibility of nuclear science experiments on OMEGA EP.³⁰

Using the deuteration technique successfully applied to MTW targets, a set of metal targets was prepared for the LBS campaign in February 2020. The unique beamline layout on OMEGA EP was exploited to obtain deuteron beam spectra with a single deuterated target in the sidelighter configuration and to perform nuclear reaction experiments with two deuterated targets in the backlighter configuration.

The OMEGA EP Thomson parabola ion energy (TPIE)³¹ analyzer was used as the main deuteron beam diagnostic for the single-target configuration, whereas the three existing nTOF scintillators were used to detect the reaction products of nuclear processes.

A striking difference between OMEGA EP deuteron beams and MTW beams is the much higher abundance of $q/m = 1/2$ species in the OMEGA EP beams. These high abundances are most likely caused by the contamination species carbon, oxygen, and nitrogen, which are pushed into their highest ionization states in the OMEGA EP experiments at laser energies >1 kJ. Titanium targets loaded with hydrogen and untreated targets were used to obtain a reliable background spectrum to be subtracted from the signal of a deuterated target. The background-corrected deuterium spectrum shown in Fig. 17 resembles the asymmetric Gaussian shape previously observed on MTW, except for increased noise due to the background. It is evident that higher laser energy predominantly increases the per deuteron energy, from below about 0.5 to ~ 5 MeV, whereas the overall yields remain similar, in the low 10^{11} deuterons per shot regime.

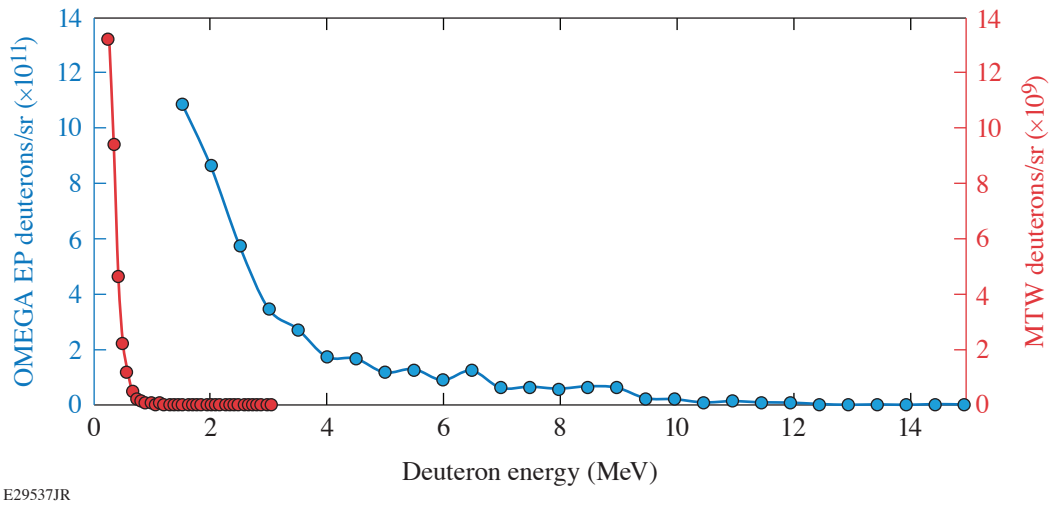


Figure 17
Deuteron spectra obtained on MTW (red circles) and OMEGA EP (blue circles) with identical targets. The corresponding Gaussian fits are represented by the solid line.

In addition, faint neutron signals were observed during experiments in the double-target configuration. Previous campaigns with deuterated plastic targets³⁰ have demonstrated that the laser parameters must be carefully adjusted for a given target to suppress the low-energy neutron background caused by (p, n) reactions in the target chamber while preserving the reaction neutrons. Further studies are planned to address this background. Figure 18 shows the neutron spectra from two different detectors at 90° and 150° for the same shot, together with Gaussian fits for the peaks that are kinematically consistent with DD fusion neutrons. While this neutron signal is quite small, just above the average noise level, the consistent observation of this signal in independent detectors indicates that these signals are real and not artifacts.

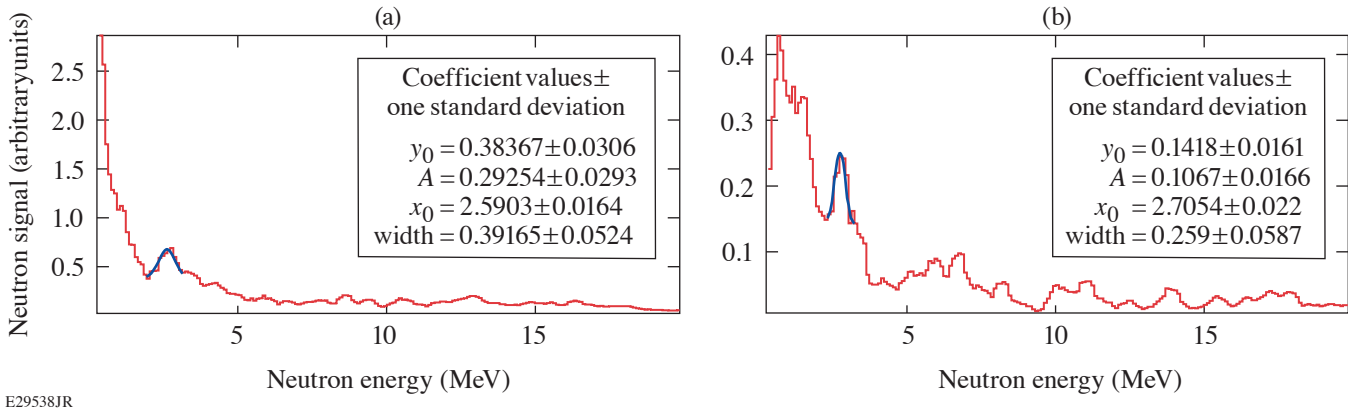


Figure 18
Neutron spectrum of shot 33407 as recorded by the nTOF at (a) 90° from the laser direction and (b) 150°. The fitted peaks are consistent with a DD fusion neutron signal assuming an effective beam energy of 1 MeV.

The experience in target preparation and laser tuning obtained in this and another planned LBS campaign will be used to produce an equivalent tritium beam in a joint shot configuration in the future.

This material is based upon work supported by the Department of Energy National Nuclear Security Administration under Award Number DE-NA0003856, the University of Rochester, and the New York State Energy Research and Development Authority.

Measurement of High-Pressure Phase-Transformation Pressures in Fe-(11 wt%)Si and MgO

Principal Investigators: R. Smith (LLNL); J. Wicks, M. Sim, and V. Rastogi (Johns Hopkins University); and X. Gong and J. R. Rygg (LLE)

The XRD-Alloy experiments on OMEGA-60 used six beams focused to 800- μm spots to dynamically compress 30- μm -thick samples of single-crystal MgO or 10- μm -thick powder samples of Fe-(11 wt%)Si over 8 ns, to pressures up to 800 GPa. Temporal laser pulse shaping delivered progressively stronger pressure to the sample over time. This ramp compression keeps the sample temperature relatively low and maintains the solid state to extreme levels of compression, avoiding the issue with shock compression where large increases in entropy increase temperatures too high to constrain exoplanet interior conditions.

The MgO or Fe-(11 wt%)Si sample was sandwiched between two single-crystal diamond foils. Diamond served as an ideal material to couple laser energy into ramp-compression waves. The diamond/MgO/diamond target was positioned on a Ta pinhole placed over the front of the PXRDIP box (power x-ray diffraction with image plates), which contains x-ray-sensitive image-plate detectors along the inner five walls (Fig. 19). The pressure history of the sample and the time of peak compression are determined by VISAR viewing the back of the sample through an aperture in the PXRDIP box. Pressure (P) and temperature (T) within the MgO sample can be simulated using the 1-D hydrocode *HYADES*, which models the coupling of the OMEGA 527-nm laser into our target geometry and calculates the 1-D hydrodynamic flow of P - T waves through the target assembly using equation-of-state descriptions of each layer.

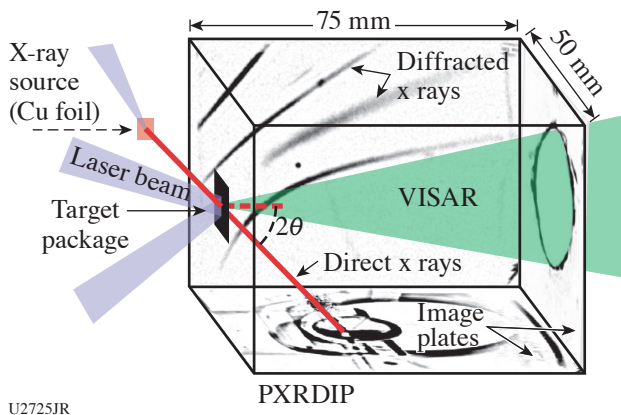


Figure 19
The PXRDIP setup on OMEGA-60.
(Figure adapted from Ref. 32).

At the time of peak compression, another 35 laser beams irradiate a Cu foil to produce a hot dense plasma of mainly He-like ions. This results in a strong quasi-monochromatic He α x-ray source over 1 ns at x-ray energies of 8.3 keV. The x rays incident onto the compressed sample scatter in a transmission-diffraction pattern, which is recorded by the image-plate detectors. Peaks from the uncompressed Ta pinhole are also recorded, providing fiducial data that allow us to plot the image-plate data as diffraction angle versus azimuthal angle around the x-ray beam axis (Fig. 20).³² The angular position of diffracted sample peaks provide direct information of the atomic lattice spacing and crystal structure at a pressure determined through VISAR. By increasing the laser intensity on target the sample pressure increases, so a systematic series of these ramp-compression x-ray diffraction shots determines the onset pressure of phase transformations.

Investigating Magnetic Fields Generated in Collisionless Plasma-Flow Interactions Using Thomson Scattering

Principal Investigators: G. F. Swadling, H. S. Park, J. S. Ross, B. Pollock, and D. Higginson (LLNL); F. Fiuza and A. Grassi (SLAC); W. Rozmus and C. Bruulsema (Dept. of Physics, University of Alberta); and H. G. Rinderknecht (LLE)

The experiments conducted for the BFieldOTS-20A OMEGA Campaign focused on investigating the generation and amplification of spontaneous magnetic fields via the Weibel filamentation instability in collisionless, interpenetrating plasmas, extending previous work recently published.³³ High-velocity (~ 1000 -km/s) streams of plasma were generated by laser heating the surfaces

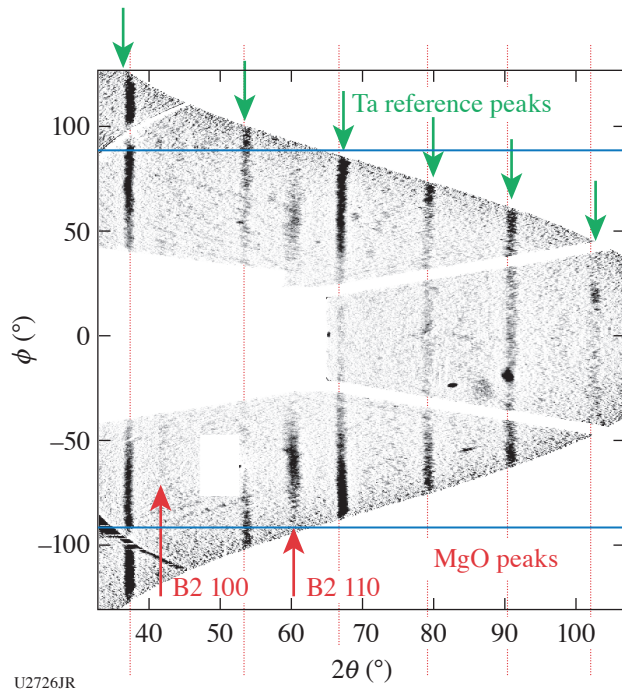


Figure 20
MgO diffraction pattern as captured on the PXRDIP image plates. The image-plate planes are projected into a linear $2\theta-\phi$ angular space with respect to the x-ray beam axis.³²

of counter-facing beryllium disk targets. The parameters of the two counterpropagating streams of plasma imply that their interactions must be collisionless: the experimental scale length is substantially smaller than the collisional mean free path expected between the two streams. For this campaign, the experiment was modified so that the targets could be driven using only the Leg 1 and 3 beams. A long-pulse Thomson-scattering probe beam driven by Leg 2 could then be used to probe the interaction for 3.7 ns, substantially longer than has previously been explored. This configuration also allowed us to carry out spatially resolved Thomson-scattering measurements using a short-pulse (100-ps) probe beam. The experiments were highly successful, data quality was excellent, and analysis is ongoing. An example of the time-resolved data is shown in Fig. 21.

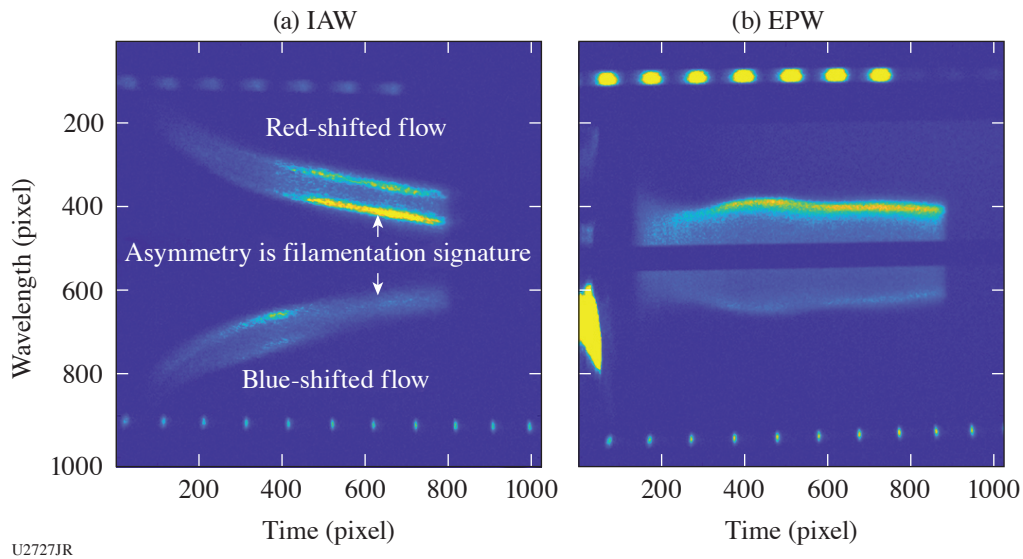


Figure 21
Example of Thomson-scattering data captured over 3.7 ns in an (a) ion-acoustic wave (IAW) and (b) electron plasma wave (EPW). The development of an asymmetry in the IAW feature is indicative of the onset of filamentation in the interpenetrating plasma.

Extreme Deformation and Failure of High Entropy Alloys by Laser Shock-Induced Compression and Tension

Principal Investigators: S. Zhao and A. Minor (LBNL); and C. Stan, C. E. Wehrenberg, and H.-S. Park (LLNL)

High-entropy alloys (HEA's) are a class of metallic alloys containing three or more elements in significant atomic proportion. They exhibit generally high-yield strength and fracture toughness and are good candidates for engineering applications such as the aerospace industry. We are interested in the spall strength behavior of these materials and studied them under shock impact to several tens of GPa. The setup consisted of three independent targets that were shot individually, one of which was a spall velocimetry target and two of which were recovery tube spall targets (Fig. 22). Recovered samples were analyzed using electron microscopy (Fig. 23).

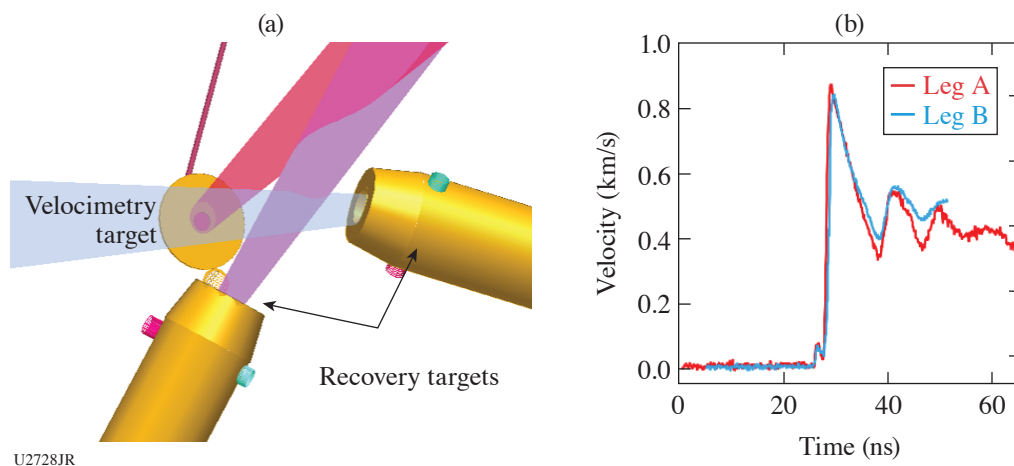


Figure 22

(a) Schematic of the experimental setup. Laser shocks were independently timed. (b) Typical spall velocimetry measurement. The beats are indicative of “ringing” in the sample, which is a marker of spall strength in samples.

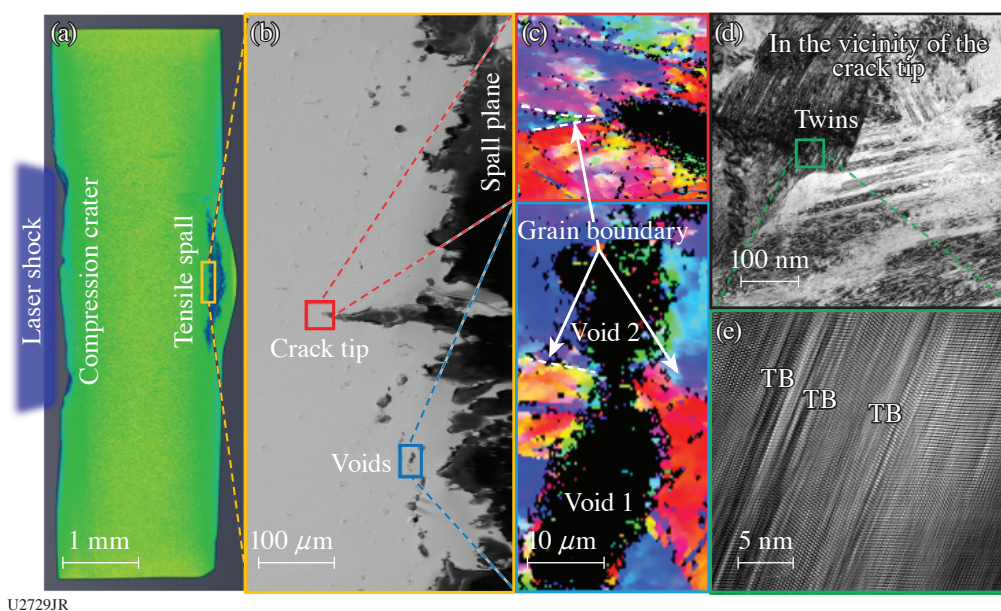


Figure 23

(a) Diagram of a spall event in a laser-driven sample. (b) Scanning electron microscopy (SEM) at the spall boundary, showing the formation of cracks and voids due to tension generated by shock unloading against vacuum. (c) Grain mapping of the crack tip, showing multiple grain boundaries. (d) Transmission electron microscopy (TEM) analysis of the grains near the crack tip, showing extensive twin formation and multiple stacking faults.

Initial analysis of the recovered samples shows that stronger shocks lead to a larger degree of plasticity. We observe stacking faults, nano twins, hexagonal-close-packed lamellae, and their interactions, with TEM. Velocimetry measurements give us an approximate spall strength of 10 GPa, which is higher than those of Ta (~8 GPa), Al (~3 GPa), or Cu (~8 GPa). Molecular dynamics simulations suggest that the strength is partially due to void pinning by twin boundaries induced during shock compression.

Implosions for Studying Solar CNO Reactions

Principal Investigators: A. B. Zylstra and J. Jeet (LLNL); Y. H. Kim (LANL); and M. Gatu Johnson (MIT)

Utilization of inertial fusion implosions to study nuclear astrophysics is a new technique popularized within the last few years.^{34,35} A particular reaction of interest is the “CNO process”³⁶ occurring in heavier stars with finite metallicity, in which hydrogen burning is catalyzed in the presence of ¹²C. These reactions are more strongly dependent on temperature, however, than the pp cycle reactions; therefore the CNO cycle dominates only in massive stars. For these types of reactions to be studied using ICF facilities, an implosion platform using heavier nuclei in the fuel and capable of creating ion temperatures of the order of at least 30 keV is required. One potential route to reach these conditions is to take advantage of kinetic effects in low-convergence, shock-driven “exploding-pusher” implosions. Ion thermal decoupling was observed in such implosions.³⁷ While the exact mechanism for shock heating is not clear (collisional versus electrostatic), a significant boost in ion temperature, up to a factor of 6 to 12× versus a hydrogen ion, is expected for carbon or heavier ions (Fig. 24). In this experiment, shots using the surrogate reaction ¹³C + D were conducted for which the cross section is substantially higher than the actual astrophysical CNO reactions. These shots were made possible by utilizing a deuterated methane gas fill. For comparison, D₂ gas fills were also used. For the implosions, 60 beams were used at 300 J per beam and a 600-ps square pulse. The targets consisted of 860-μm-diam shells (CH) at thicknesses of 5.7 and 7.1 μm.

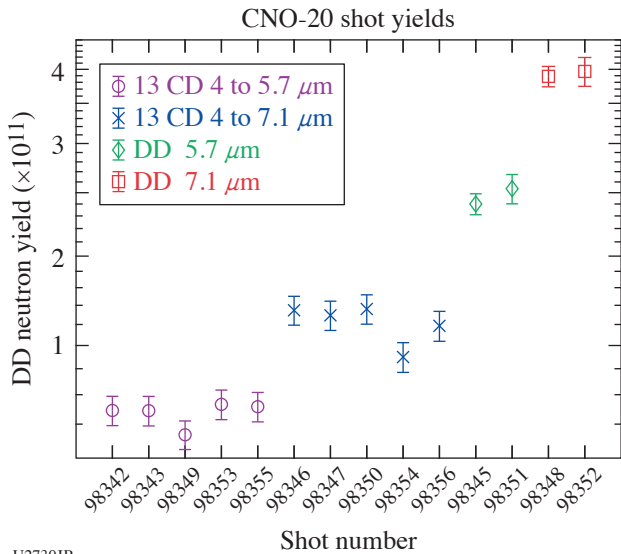


Figure 24
D–D ion temperatures versus fuel type and shell thickness as determined from the neutronics diagnostics. The deuterated methane targets achieve a larger ion temperature. For each fuel type, the smaller shell thickness results in a larger ion temperature.

The ¹³C + D neutron yield was expected to be low (as shown in Fig. 25), and the nTOF data show no clear signature of the 5-MeV neutrons. The DAD data do show a gamma-ray signal, but it is unclear if this is due to carbon gammas. The primary diagnostics include the CPS, wedge-range filters (WRF’s), and SRF’s to measure the ¹³C + D protons. The CR-39 is currently being processed to determine the proton yield and energy spectrum. The results will inform whether kinetic effects can boost high-Z reaction yields and will provide a basis for designing future CNO experiments.

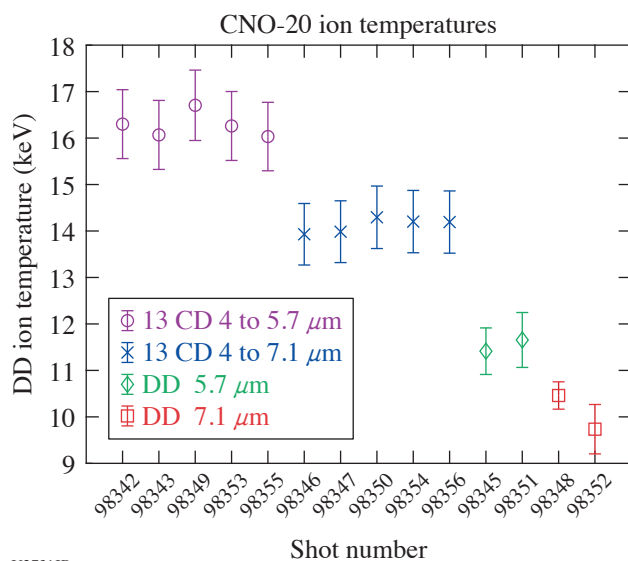


Figure 25

D–D neutron yields versus fuel type and shell thickness as determined from the neutronics diagnostics. The deuterated methane targets have a lower D–D neutron yield. For each target gas-fill type (D_2 and $^{13}\text{C} + \text{D}$), the smaller shell thickness results in a lower D–D neutron yield.

REFERENCES

1. H. Chen *et al.*, Phys. Rev. Lett. **114**, 215001 (2015).
2. H. Chen *et al.*, Phys. Plasmas **21**, 040703 (2014).
3. G. Fiksel *et al.*, Bull. Am. Phys. Soc. **64**, NO08.00010 (2020).
4. S. Root *et al.*, Geophys. Res. Lett. **45**, 3865 (2018).
5. D. E. Fratanduono *et al.*, Phys. Rev. B **97**, 214105 (2018).
6. S. Stewart *et al.*, AIP Conf. Proc. **2272**, 080003 (2020).
7. S.-N. Luo *et al.*, J. Geophys. Res. Solid Earth **109**, B05205 (2004).
8. C. Wang *et al.*, Phys. Plasmas **22**, 102702 (2015).
9. V. A. Thomas and R. J. Kares, Phys. Rev. Lett. **109**, 075004 (2012).
10. D. S. Clark *et al.*, Phys. Plasmas **23**, 056302 (2016).
11. R. I. Klein *et al.*, Astrophys. J. **583**, 245 (2003).
12. V. V. Korobkin and S. L. Motylev, Sov. Tech. Phys. Lett. **5**, 474 (1979).
13. G. Fiksel *et al.*, Appl. Phys. Lett. **109**, 134103 (2016).
14. M. Millot *et al.*, Nat. Phys. **14**, 297 (2018).

15. M. Millot *et al.*, *Nature* **569**, 251 (2019).
16. S. Brygoo *et al.*, *J. Appl. Phys.* **118**, 195901 (2015).
17. S. A. Slutz *et al.*, *Phys. Plasmas* **17**, 056303 (2010).
18. D. B. Schaeffer *et al.*, *Phys. Rev. Lett.* **119**, 025001 (2017).
19. W. Fox *et al.*, *Physics Archive*, <https://arxiv.org/abs/2003.06351> (2020).
20. A. Valenzuela *et al.*, *Nature* **320**, 700 (1986).
21. D. D. Ryutov *et al.*, *Phys. Plasmas* **19**, 062706 (2012).
22. L. Ballabio, J. Källne, and G. Gorini, *Nucl. Fusion* **38**, 1723 (1998).
23. K. Molvig *et al.*, *Phys. Rev. Lett.* **109**, 095001 (2012).
24. J. D. Huba, NRL Plasma Formulary, Naval Research Laboratory, Washington, DC, D 210.2:P 69/4/2009 (2009).
25. W. T. Taitano *et al.*, *Phys. Plasmas* **25**, 056310 (2018).
26. L. Torrioni *et al.*, *Phys. Scr.* **T161**, 014026 (2014).
27. J. T. Morrison *et al.*, *Phys. Plasmas* **19**, 030707 (2012).
28. S. Karsch *et al.*, *Phys. Rev. Lett.* **91**, 015001 (2003).
29. A. Schwemmlin *et al.*, “Optimizing Deuterated Metal Foils to Generate a High-Yield, Quasi-Monoenergetic Deuteron Beam Employing Target Normal Sheath Acceleration on the Multi-Terawatt Laser System at the Laboratory for Laser Energetics,” to be submitted to *Nuclear Instruments and Methods A*.
30. C. Stoeckl *et al.*, *Nucl. Instrum. Methods Phys. Res. B* **453**, 41 (2019).
31. C. C. Freeman *et al.*, *Rev. Sci. Instrum.* **82**, 073301 (2011).
32. J. K. Wicks *et al.*, *Sci. Adv.* **4**, eaao5864 (2018).
33. G. F. Swadling *et al.*, *Phys. Rev. Lett.* **124**, 215001 (2020).
34. A. B. Zylstra *et al.*, *Phys. Rev. Lett.* **117**, 035002 (2016).
35. A. B. Zylstra *et al.*, *Phys. Rev. C* **101**, 042802(R) (2020).
36. H. A. Bethe, *Phys. Rev.* **55**, 434 (1939).
37. H. G. Rinderknecht *et al.*, *Phys. Rev. Lett.* **114**, 025001 (2015).